

MAPAN-JOURNAL ,
Publisher: METROLOGY SOC INDIA ,
NPL PREMISES,
Address: DR K S KRISHNAN MARG,
NEW DELHI, INDIA,
ISSN / eISSN:0970-3950 / 0974-9853
Volume 25-Issue 1-(2025)



Type of the Paper (Article, Review, Communication, etc.)

# Study on Geological Hazard Identification in Qinghai Province Based on LT-1 InSAR Data (A) Check for updates

Zongren Li 1,2,3, DeLin Li 1,2,3,\*, Yonglian Sha 1,2,3, Na Zhang 1,2,3, Xing Zhang 1,2,3, Huijun Qi 1,2,3, and Baicheng Feng 4

- <sup>1</sup> Qinghai Provincial Institute of Geological Survey, Xining 810012, China; 303523234@qq.com
- <sup>2</sup> Qinghai Provincial Remote Sensing Big Data Engineering Technology Research Center, Xining 810012, China
- <sup>3</sup> Key Laboratory of Geological Processes and Mineral Resources of the Northern Tibetan Plateau, Xining 810012, China
- Moonbristar (Beijing) Technology Co., Ltd, Beijing 100080, China
- \* Correspondence: 104014137@qq.com

#### Funding:

Qinghai Provincial Bureau of Geology and Mineral Exploration Planned Project: "Research on Key Technologies for Remote Sensing Integrated Identification of Geological Hazard Potential Based on Domestic Land Exploration Satellite SAR Data (2024-24-4)"

Qinghai Provincial Bureau of Geology and Mineral Exploration Planned Project: "Research on Key Technologies for AI-Based Identification of Geological Hazard Potential Using Multi-Source Remote Sensing (2025-17-2)"

**Abstract:** LT-1 SAR satellite is the first L-band full polarization civil SAR constellation in China. It consists of two SAR satellites with the same parameters. The revisit period can reach 4 days in follow-up mode. It has the advantages of high resolution, short revisit period and full polarization imaging, which is beneficial to the monitoring and identification of geological hazards in complex areas. Affected by the warm and humid Qinghai-Tibet Plateau, extreme rainfall weather occurs frequently in Qinghai Province, and there is an increasing trend, forming regional and mass geological disasters of collapse, landslide and debris flow, causing road interruption, house and farmland damage, etc., seriously threatening people's life and property safety and causing huge economic losses. Firstly, SBAS technology is used to solve the problem in the study area. According to the characteristics of large relief and distributed scatterers in the study area, the terrain residual error removal algorithm based on M estimation and the deformation sequence solution algorithm based on ridge regression and residual decomposition are proposed respectively. Then, based on the multi-scene LT-1 data, the improved SBAS-InSAR technology was used to monitor the surface deformation in the area of about 590 km2 in Xining City and Haidong City of Qinghai Province from July 2023 to December 2024, and the geological hazard hidden danger points were identified by combining the optical images and DEM data of the corresponding areas. Meanwhile, the identified four typical hidden danger areas were compared and analyzed in combination with the existing geological hazard hidden danger database. The results show that the maximum accumulated deformation of hidden danger area exceeds 100mm, which proves that LT-1 can provide abundant data support for disaster prevention and mitigation, and provides a case reference for the application of improved SBAS-InSAR technology in geological disaster monitoring.

**Keywords:** LT-1; microwave remote sensing; DInSAR; early recognition of geological hazards

Academic Editor: Firstname Lastname

Received: date Revised: date Accepted: date Published: date

**Citation:** To be added by editorial staff during production.

Copyright: © 2025 by the authors. Submitted for possible open access publication under the terms and conditions of the Creative Commons Attribution (CC BY) license (https://creativecommons.org/licenses/by/4.0/).

#### 1. Introduction

Geological hazards are natural disasters dominated by geological dynamic activities or abnormal changes in geological environment, including mountain collapse, landslide, debris flow, ground collapse, ground fissure subsidence and uplift caused by natural factors or artificial activities. Continuously improving the ability of geological hazard hidden danger and geological structure discovery based on remote sensing identification and investigation evaluation, and geological hazard monitoring and early warning ability based on "civil air defense + technical prevention" are the keys to reduce geological hazard risk and improve the timeliness and coverage of geological hazard early warning. Compared with the commonly used GNSS monitoring, total station monitoring, deep displacement measurement, leveling, deformation automatic monitoring and other geological hazard monitoring technologies [1-2], InSAR technology has become a major means of topographic deformation measurement, and is one of the frontier technologies that have developed rapidly in recent 30 years [3-4].

DInSAR is a technology that uses two SAR images of the same area at different times for coherent processing to obtain corresponding surface deformation information. It has the advantages of large range, high accuracy, all-day and all-weather [5-6]. Because DIn-SAR technology has serious space-time coherence loss under the condition of large spatial baseline or long time interval, it cannot obtain effective deformation information, and its application has received certain restrictions. PSInSAR technology proposed later selects stable PS points for time series InSAR processing by using long time series images, and only extracts deformation parameters at these stable points, which effectively improves deformation inversion ability [7-10]; SBAS technology uses multi-reference image mode to generate interferogram under the limitation of specified time baseline and spatial baseline threshold, and performs multi-view processing on interferogram to improve signalto-noise ratio, and then processes unwrapped phase model by SVD technology to obtain deformation information [11-13]; The time-series InSAR technique based on distributed scatterer processing uses the homogeneous points identified by statistical test method for phase optimization [14] to improve signal-to-noise ratio, and does not sacrifice image resolution like SBAS. For the optimized phase, conventional time-series InSAR technique can be used to retrieve deformation [15-17]. Various InSAR deformation monitoring techniques have been widely used in Kuangqu subsidence [18-21], urban groundwater extraction [22-23], geological hazard monitoring [24-26], seismic coseismic field inversion [27-30], glacier drift [31-34] and other fields.

For a long time, the InSAR data used were all from foreign open source and commercial SAR satellites, such as Sentinel1, ALOS-1/2, TerraSAR-X/Tandem-X, RadarSAR-1/2, Cosmo-SkyMed, etc. Currently, the mainstream L-band SAR satellites used for surface deformation monitoring are Japan's ALOS-2 and Argentina's SAOCOM-1 satellites, while LT1 satellite is China's first group of L-band fully polarized civil SAR satellite constellation with interference as its core mission. It consists of A and B binaries, which can carry out two flight modes of follow-up and fly-around in orbit, and have the observation capability of single satellite 8d and double satellite 4d repeated orbit. LT-1 was officially put into use on December 29, 2023, marking that the constellation can provide large-range, high-precision, autonomous and controllable interferometric SAR data, changing the dependence on foreign commercial satellites in the past. Compared with X and C bands, L-band wavelength used by LT-1 is longer, and its ability to penetrate vegetation is stronger, which is conducive to obtaining ground information. At present, a large number of scholars have studied the processing and application of L-probe-1 [35-36].

Based on the multi-scene SAR data of Litan-1, the deformation results of some regions in Qinghai Province are obtained by using improved SBAS-InSAR technology, and

the hidden danger points of geological hazards are identified by combining the optical images and DEM data of corresponding regions. Section 2 introduces InSAR processing technology and data processing process; Section 3 analyzes the experimental results; Section 4 summarizes and prospects the whole paper.

# 2. Introduction to the Study Area and Data

#### 2.1. Introduction to the Study Area

Qinghai Province is located in the western part of China, northeast of the Qinghai-Tibetan Plateau. It is the birthplace of the Yangtze River, the Yellow River and the Lancang River, and is known as the "source of the three rivers", "the source of the rivers" and "the Chinese water tower". The terrain is characterized by a combination of high south-west, low north-east and high north-south, low central and many mountains and few plains. Within the area, there are the world's highest elevation, the latest era of uplift, the largest crustal thickness, as the foundation of the Tibetan Plateau and the preservation of the world's highest plateau surface and tectonic mountain system. The region has complex geological and environmental conditions, fragile ecology, diverse climate and frequent earthquakes. The landscape is dominated by mountains and hills, accounting for 72% of the province's area. Strong uplift of the plateau and river erosion, resulting in the region's terrain, gullies and ravines, steep valley slopes, in the mountains, hills, plateaus and river plains in the transition zone, geologic hazards in a relatively concentrated and strip distribution, with a wide range, the number of groups of emergencies, the severity of the disaster, the management of the difficulty and other characteristics.

In recent years, under the influence of warming and humidification of the Qinghai-Tibetan Plateau, regional extreme rainfall weather is frequent, and the annual precipitation also has a tendency to increase, which is prone to triggering widespread mass geological disasters, especially in recent years due to the rainfall triggered by the sudden, mass geological disasters are unusually frequent. The amount of rainfall has been the highest daily precipitation in the history of each region since the beginning of meteorological records, and these heavy rainfalls have caused regional and mass collapses, land-slides and mudslides, seriously threatening the safety of people's lives and properties, causing road disruptions, damage to houses and farmland, etc., and resulting in huge economic losses.

Xining City is located in the east of Qinghai Province, northeast of the Tibetan Plateau, located in Huangshui and its three tributaries of the confluence. City elevation of 2261 meters, was east-west strip, the terrain southwest high, northeast low. Surrounded by mountains, Huangshui River through the city. Geographic coordinates between  $100\,^\circ$  52-  $101\,^\circ$  54' east longitude, latitude  $36\,^\circ$  13' -  $37\,^\circ$  28' between. Haidong city is located in the east of the Qinghai Lake and named, is a semi-arid continental climate, is located in the Qilian Mountain tributary of the southern foot of the Daban Mountain and the Kunlun Mountains system of the remnants of the eastern slopes of the Riyue Mountain, belongs to the Loess Plateau to the Tibetan Plateau transition mosaic, the elevation of 1,650 ~ 2,835 meters between. The territory is characterized by rolling hills and ditches. Figure 1 shows the geographic location of Xining and Haidong cities in Qinghai Province.

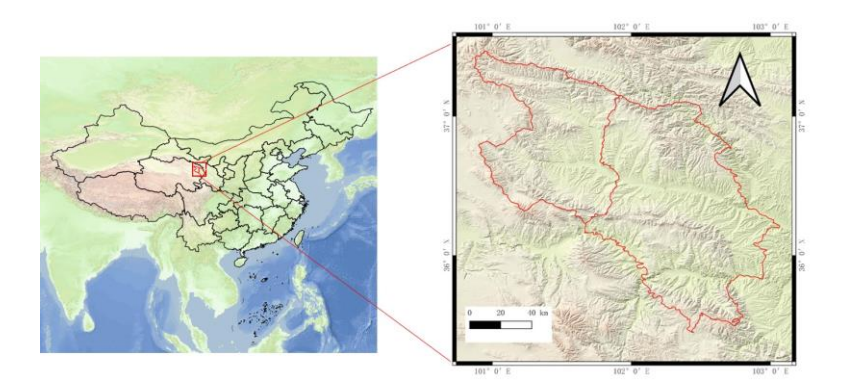


Figure 1. Geographic location map of the study area.

#### 2.2. Data Introduction

The L-band differential interferometric SAR satellite [37] is China's first L-band fully polarized satellite constellation with interferometry as its core mission, i.e., LT-1 consists of two identical satellites, Star A and Star B, with dual star orbiting and dual star following modes. LT-1 consists of two identical satellites, Star A and Star B, with two-star orbiting and two-star following modes. In the dual-star orbiting mode, the satellites fly synchronously in a double-helix structure at a distance of 700-7000m, which is mainly used for InSAR measurements to obtain surface elevation information. In the two-star following mode, the satellite flies back and forth with 180° orbital spacing, and its return orbit control radius reaches 350m, which is mainly used for obtaining surface deformation information.

The orbit of LT-1 is a sun-synchronous orbit with a satellite altitude of about 607km, which can photograph land areas within the global latitude range of 85 degrees north and south. The satellite re-defense cycle is 8 days for a single star and 4 days for a double-star joint revisit cycle. LT-1 contains six imaging modes, and its imaging modes and main technical parameters are shown in Table 1.

Table 1 Imaging modes and main technical parameters of LT-1

Serial	Imaging	Resolution	Swath width	Incidence	Polarization
number	mode	(m)	(km)	angle (°)	mode
1	STRIP1	3	50	20 ~ 46	HH or VV
2	STRIP2	12	100	20 ~ 46	HH or VV
3	STRIP3	3	50	10 ~ 60	HH+HV or VV+VH
4	STRIP4	6	30	13 ~ 21	HH+HV+VH+VV
5	STRIP5	24	160	15.7 ~ 30	HH or VV
6	SCAN	30	400	20 ~ 49	HH or VV

LT-1 can be used for natural resources investigation, emergency management and forestry and grassland monitoring, and serves such industries as geology, land, surveying and mapping, disaster mitigation, earthquake and forestry and grassland. The L-band wavelength used by LT-1 is longer, which is more capable of penetrating the vegetation and is conducive to the acquisition of ground information. A total of 11 scenes of SAR data are used in this experiment, the data coverage is shown in Figure 2, and the key parameters of the data are shown in Table 2.

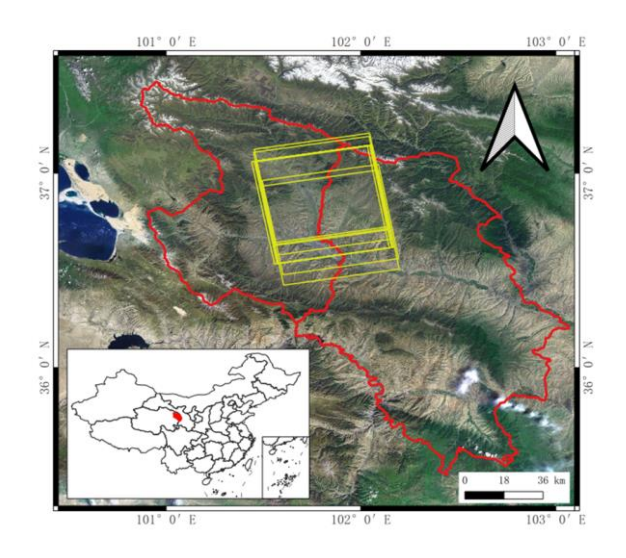


Figure 2. Coverage of LT-1 SAR imagery used in the study area.

Table 2 Imaging modes and main technical parameters of LT-1

Serial number	Orbit number	Acquisition date	Ascending and de- scending orbit	Incidence angle (°)	Polariza- tion mode
1	7802	2023/07/04	Ascending orbit	39.4132	НН
2	8218	2023/09/02	Ascending orbit	39.4556	НН
3	9111	2023/09/30	Ascending orbit	39.5015	НН
4	10777	2024/01/20	Ascending orbit	39.4220	НН
5	10717	2024/02/17	Ascending orbit	39.4314	НН
6	11610	2024/03/16	Ascending orbit	39.4196	НН
7	11550	2024/04/13	Ascending orbit	39.4195	НН
8	12443	2024/05/11	Ascending orbit	39.2858	НН
9	13276	2024/07/06	Ascending orbit	39.4446	НН
10	14882	2024/11/23	Ascending orbit	39.4385	НН
11	15774	2024/12/21	Ascending orbit	39.3931	НН

The Sentinel-1 satellite project is the first of the five Copernicus programs proposed by ESA and the European Community in 2005, which is dedicated to high-resolution and large-area coverage monitoring of the global land and oceans, and is a dual-constellation satellite consisting of Sentinel-1A, which was launched in April 2014, and two subsequent satellites, Sentinel-1B, which were launched in April 2016, sharing the same near-polar sun-synchronous orbit plane to achieve a short re-entry cycle. The project is a dual con-

stellation of satellites, including Sentinel-1A, which was launched in April 2014, and Sentinel-1B, which was launched in April 2016. The two satellites share the plane of the nearpolar sun-synchronous orbit in order to realize a short re-entry cycle, with an orbital altitude of 693km and an inclination angle of 12 days for a single satellite after the operation of the satellite system is stabilized and a re-entry cycle of 6 days for the constellation, so as to achieve uninterrupted imaging in all-weather and with high coverage throughout the year. The constellation is equipped with a C-band advanced SAR detection system with a wavelength of 5.6cm, a wide ground monitoring range, continuous monitoring time, multiple imaging modes and strict orbit control technology, which is very suitable for research related to time series InSAR technology.

A total of 38 views of Sentinel-1A data were used in this experiment, with data coverage from July 11, 2023 to December 20, 2024 as shown in Figure 3.

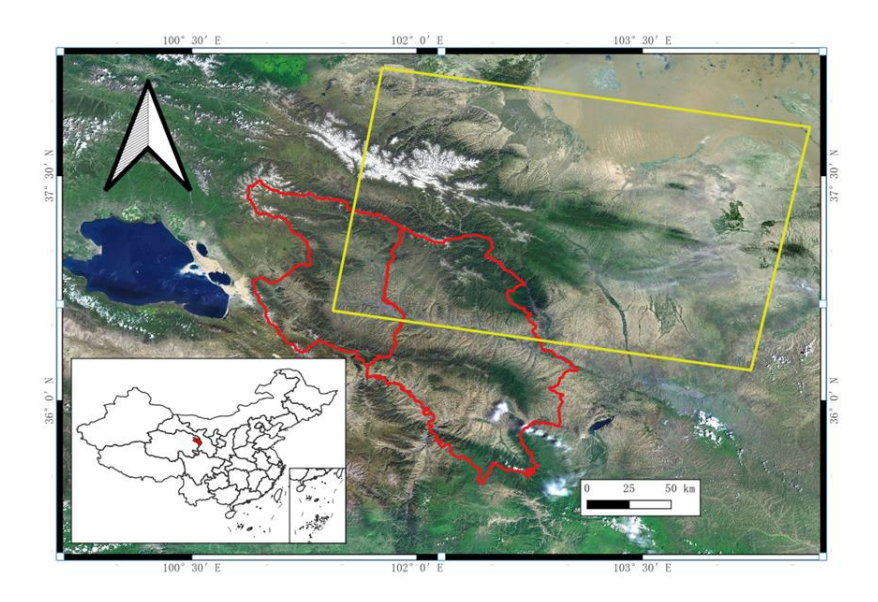


Figure 3. Sentinel-1ASAR image coverage used in the study area.

The ALOS World 3D-30m dataset is a global digital surface model (DSM) with a horizontal resolution of approximately 30 meters (1 arcsecond). It was acquired by the Panchromatic Remote-sensing Instrument for Stereo Mapping (PRISM) aboard the Advanced Land Observing Satellite (ALOS), a high-resolution stereo mapping sensor. Detailed information about the dataset is shown in Table 4.

Table 3. This is a table. Tables should be placed in the main text near to the first time they are cited.

Information	Content
Product Name	ALOS World 3D – 30m (AW3D30) Version 2.2
Resolution	1 arc second (about 30 meters)
File unit (single file size)	1×1 degree slice
File Type	Digital Surface Model(DSM)
File composition	MSK file: mask information (cloud and snow, land and water and low correlation, ocean, DEM information, for supplemental processing); STK file: DSM data stack used to generate AW3DDSM data source; QAI file: data quality information; HDR file: product metadata;

# 3. Data processing method

# 3.1. Differential Interference Technology

The fundamental principle of radar interferometry lies in utilizing the phase differences between multiple Synthetic Aperture Radar (SAR) image datasets to calculate surface elevation deformations. When the elevation of ground objects at the same location changes, the phase reflected in the SAR image pixels undergoes corresponding changes, where the phase change corresponds to the radar echo distance between the satellite antenna and the ground objects. Through precise measurement and processing of these phase differences, the elevation changes at each point on the surface can be calculated. This process involves multiple complex steps, including:

- Image registration: Ensuring that the pixels of SAR images acquired at different times or by different antennas can be accurately matched.
- Interferogram formation: Deriving phase differences through complex conjugate multiplication.
- Phase unwrapping: Obtaining complete phase information by resolving full cycle counts.
  - Flat-earth effect removal and noise filtering: Enhancing data accuracy and reliability.

Through these processing steps, high-resolution and high-precision surface elevation data can ultimately be obtained. According to different approaches for acquiring Digital Elevation Models (DEM), it can be classified into the two-track method, three-track method, and four-track method. The workflow for geological hazard identification based on Differential Interferometric Synthetic Aperture Radar (DInSAR) technology is shown in Figure 4, which is generally divided into three parts: data preprocessing, DInSAR deformation inversion, and potential hazard point identification.

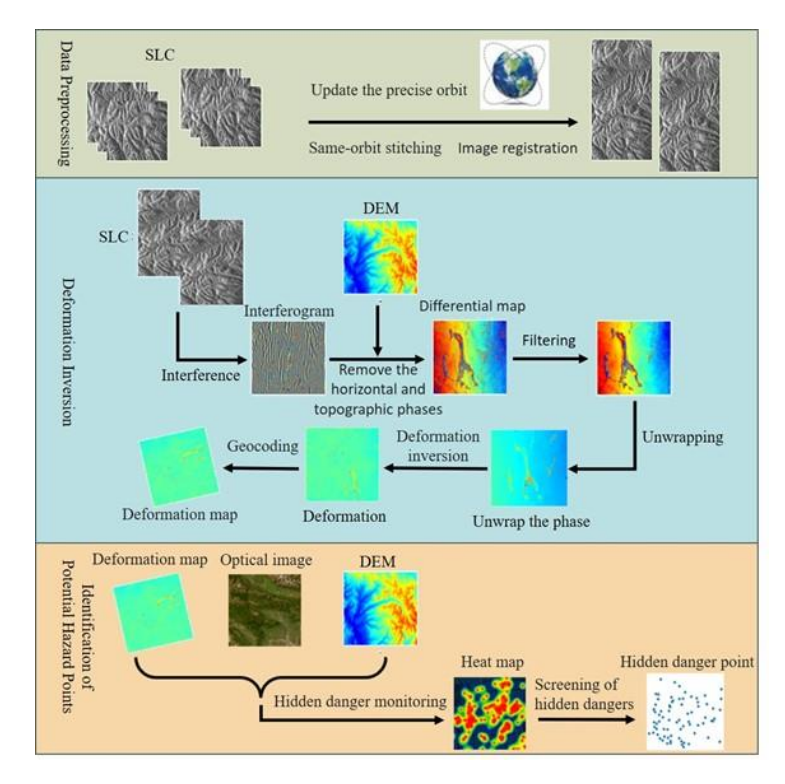


Figure 4. Flow chart of geological disaster identification based on DInSAR technology.

When the surface undergoes deformation between two imaging periods, the interferometric phase becomes complex. It not only carries critical information about surface deformation. To accurately extract surface deformation information, precise analysis and processing of the interferometric phase are required to eliminate or reduce the influence of non-deformation phase components. The resulting interferometric phase  $\Delta \phi$  can be expressed as:

$$\Delta \varphi = \varphi_{\text{flat}} + \varphi_{\text{topo}} + \varphi_{\text{def}} + \varphi_{\text{aps}} + \varphi_{\text{noise}} \tag{1}$$

Among them,  $\varphi$ \_flat is the flat-earth phase component, also known as the reference plane phase, which is caused by the phase differences of different points on the reference plane;  $\varphi$ \_topo is the topographic phase component, which reflects the topographic height of the target;  $\varphi$ \_def is the deformation phase component. It should be noted that its direction is along the radar line-of-sight direction;  $\varphi$ \_aps is the atmospheric phase component, and the signal transmission is affected by the ionosphere and the troposphere;  $\varphi$ \_noise is the random noise. According to the estimated spatial baseline and imaging parameter information, the flat-earth phase is simulated and removed from the interferogram; the simulated phase generated by using the external reference DEM is used to remove the topographic phase from the interferogram, and this step is also called the secondary differential; the interferogram is filtered to reduce the noise and accelerate the phase unwrapping speed. A commonly used method is the Goldstein adaptive filtering; the filtered interferogram is subjected to phase unwrapping to restore the absolute phase information, that is,

$$\Phi_{\text{unw}} = \varphi_{\text{intf}} + 2k\pi, k = 0, \pm 1, \pm 2, ...$$
(2)

Among them,  $\phi_{-}$  intf represents the wrapped phase,  $\Phi_{-}$  unw is the unwrapped absolute phase. Phase unwrapping recovers the ambiguous phase number k. Commonly used methods include minimum cost flow phase unwrapping and branch cut phase unwrapping, etc.; Convert the unwrapped phase into the amount of deformation,  $\phi_{-}$  def=- $4\pi/\lambda$ - $\Delta r$ , where  $\Delta r$  represents the amount of deformation along the radar line-of-sight direction; Geocode the deformation result, converting from the SAR coordinate system to the geographic coordinate system.

With the continuous development of radar satellite technology, more complex noises appear in the process of processing high spatial resolution images. However, the traditional D-InSAR technology hardly achieves matching millimeter-level measurement accuracy and is prone to distortion due to horizontal deformation. Considering the influences of terrain, atmosphere and other factors, researchers have further improved the previous D-InSAR technology and proposed time-series InSAR technology to eliminate the impacts of atmospheric delay, spatio-temporal incoherence and other factors. Among them, the small baseline subsets InSAR (SBAS-InSAR) and persistent scatterer InSAR (PS-InSAR) technologies are more common.

#### 3.2. The improved SBAS technique

SBAS-InSAR is an interferometric measurement method that uses interferometric image pairs with both temporal and spatial baselines smaller than a given threshold to form multiple differential interferogram sets, and conducts a time-series analysis of the differential phase sequences of coherent pixels to obtain the time-series deformation amounts of coherent pixels.

Bernardino et al. and Lanari et al. proposed the SBAS (Small Baseline Subset) method for detecting surface deformation. The SBAS method divides all the SAR images covering the same area into several subsets. The baseline distances (including temporal baseline

distances and spatial baseline distances) of the images within each subset are relatively small, while the baseline distances between subsets are relatively large.

If all the images belong to a single small baseline set, the deformation phase can be obtained using the least squares method. However, in reality, this possibility is very small, and all the available images are usually divided into several subsets. Therefore, in order to increase the temporal sampling frequency of the deformation signal, we are faced with the situation where the data exists in different baseline sets. The matrix A is rank-deficient, and  $A^TA$  is a singular matrix. Thus, assuming there are L different small baseline sets, the rank of A is N-L+1, and the equation will have an infinite number of solutions (we assume that  $N \leq M$ ; the same assumption is made for other examples).

The generalized inverse of matrix A is obtained through the Singular Value Decomposition (SVD) method, thereby giving the least squares solution in the sense of the minimum norm for the following equation.

In particular, we decompose the matrix A through the Singular Value Decomposition (SVD) as follows:

$$A=USV^{T}$$
 (3)

Here, U is an  $M \times M$  orthogonal matrix, and its first N rows are the eigenvectors of  $AA^T$ , which are called the left singular vectors of A. V is an  $N \times M$  unitary matrix, and all of its rows are the eigenvectors of  $A^TA$ , which are called the right singular vectors of A. S is an  $M \times M$  matrix, and its elements (singular values  $\sigma_i$ ) are the square roots of the corresponding eigenvalues of the  $M \times M$  matrix  $AA^T$ . Usually, M > N, and there are M - N eigenvalues equal to 0. In addition, due to the rank-deficient property of matrix A, there are L-1 additional eigenvalues equal to 0. In summary:

$$S = diag\left(\sigma_{1}, \dots, \sigma_{N-L+1}, 0 \dots, 0\right) \tag{4}$$

Under the least - squares constraint, finding  $\Phi$  can be expressed as follows:

$$\hat{\phi} = A^{+} \delta \phi \tag{5}$$

Among them,  $A^+ = VS^+U^T$ 

In the formula,  $S^+ = diag(1/\sigma_1,...,1/\sigma_{N-L+1},0...,0)$  and thus we have:

$$\hat{\phi} = \sum_{i=1}^{N-L+1} \frac{\delta \phi^{\mathrm{T}} u_i}{\sigma_i} v_i \tag{6}$$

Here,  $u_i$  and  $v_i$  are the row vectors of U and V respectively.

In order to obtain a reliable solution with physical significance, we transform the unknown quantities in Equation (7) into the average phase rate of adjacent time observations. Correspondingly, the new unknown quantities are:

$$\underline{v}^{T} = \left[ \frac{\phi_{1}}{t_{1} - t_{0}}, \dots, \frac{\phi_{N} - \phi_{N-1}}{t_{N} - t_{N-1}} \right]$$
 (7)

Equation (8) becomes:

$$\sum_{k=IS_{j}+1}^{IE_{j}} (t_{k} - t_{k-1}) v_{k} = \delta \phi_{j}, \forall j = 1, ..., M$$
(8)

Expressed in matrix form, the following equation can be obtained.

$$Bv = \delta\phi \tag{9}$$

B is an M×N matrix. For the general term (j, k), B(j, k)=tk+1-tk when  $IS_j$ +1 $\le$ k $\le$  $IE_j$ ,  $\forall j$  =1,...,M, and D(j, k)=0 otherwise. Of course, by performing singular value decomposition on the matrix B, the minimum - norm solution of the velocity vector v can be obtained, and the result is continuous.

The SBAS data processing flow mainly includes data preprocessing, differential interferometric calculation, estimation of temporal and spatial deformation amounts, calculation of deformation amounts, etc. The SBAS technology is adopted to calculate the study area. According to the characteristics of large topographic undulations and a large number of distributed scatterers in the study area, an algorithm for removing topographic residual errors based on M-estimation and an algorithm for solving the deformation sequence based on ridge regression and residual decomposition are respectively proposed in the calculation process.

An algorithm for removing topographic residual errors based on M-estimation is proposed. The threshold screening method is used to select the pixel points whose intensity and coherence are both higher than the specified thresholds as control points. The elevation information and unwrapped phases of the control points are extracted. According to the interferometric geometric model, a system of equations of the spatial baseline, unwrapped phase and DEM is constructed. The refined baseline is obtained by solving the system of equations through M-estimation. M-estimation can effectively deal with the interference of outliers and obtain more robust parameter estimation. The estimated precise baseline can be used to effectively estimate and remove the residual topographic phase errors.

An algorithm for solving the deformation sequence based on ridge regression and residual decomposition is proposed. According to the fact that the components of the time-series interferometric phase model consist of elevation correction, linear deformation and residual phase, a regression equation of the unwrapped phase, temporal baseline and spatial baseline is constructed. The linear deformation and elevation correction are obtained by solving the system of equations through ridge regression. Ridge regression introduces regularization to achieve high numerical stability, thus obtaining high calculation accuracy and effectively solving the phase deviation problem of SBAS. After solving the linear deformation and elevation correction, the PCA method is used to separate the residual phase model from the residual errors. Finally, the non-linear deformation is filtered out through spatio-temporal filtering, and the time-series deformation is obtained by combining the linear deformation and non-linear deformation.

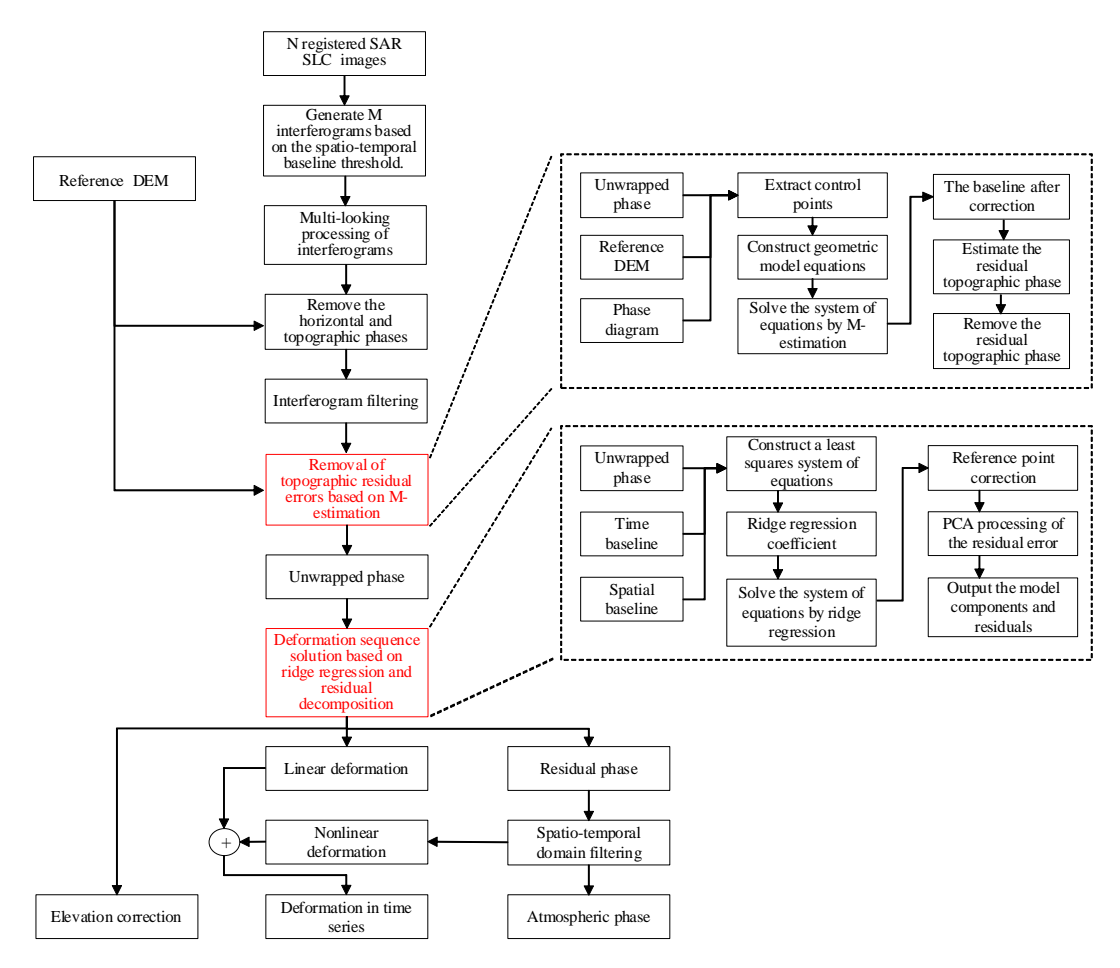


Figure 5. Basic Data Processing Flow Chart of SBAS-InSAR Technology.

# 4. Geological disaster potential identification results

#### 4.1. Data processing flow

This paper mainly uses SBAS technology to obtain surface deformation information in the research area. Since the amount of LT-1 data is relatively small, although its spatial baseline is poor, all of this data is still retained, and the image from 2024-01-20 is selected as the main image. Finally, 22 interference maps were obtained, and the spatiotemporal baseline distribution was shown in Figure 5. The spatial and temporal filtering method is used to separate and eliminate terrain errors, track errors, atmospheric errors and other errors; the three-dimensional phase unwrap method of space-time and time is used to unwrap the interference map to obtain surface deformation information. Due to the lack of satellite images in other orbits, the acquired SAR images are processed using SBAS-InSAR technology. Select the image from 2024-01-20 as the main image, and set the time and space baseline thresholds to 150d and ±1500m respectively.

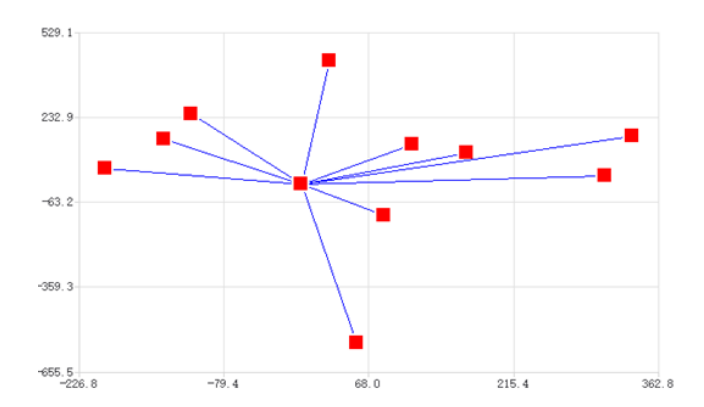
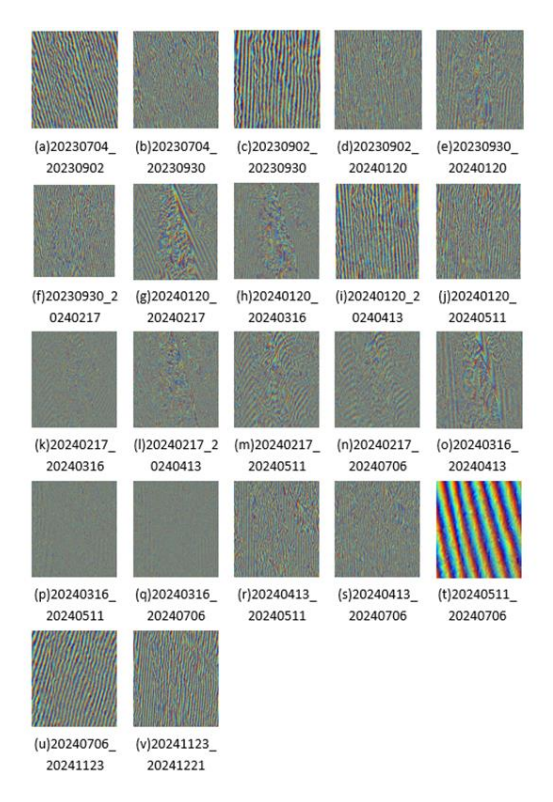


Figure 6. Spatial-temporal baseline distribution map of study area.

In the InSAR data processing process, key operations are first required for the main and auxiliary images. The main image is used as the reference and the auxiliary image is paired with it. The corresponding pixels of the main and auxiliary images are conjugated and multiplied to achieve the extraction of phase information. After completing the conjugate multiplication, the interference result is then calculated. In this data processing, after strict screening and processing, 22 pairs of interference were successfully obtained. Each pair of interference pairs contains deformation information of the target area under specific spatial and temporal conditions, and these information are contained in the interference results in the form of phase difference. The final interference diagram is shown in Figure 7. The interference diagram intuitively presents the phase differences in different regions in the form of stripes. In the future, in-depth deformation analysis and interpretation can be carried out based on these stripes characteristics.



**Figure 7.** Interference map of the study area.

After obtaining the interference map, we will enter the key data processing step. First, the phase removal operation between the flat and terrain is carried out. The reason for this step is that the original interference map contains phase information caused by factors

such as the curvature of the earth and the undulation of the terrain. This information is not generated by the target deformation and will interfere with subsequent analysis. These non-deformation-related phases are accurately calculated and eliminated to generate differential interference phases. On this basis, each cell is carefully calculated and a differential interference map is finally generated. After the differential interference map is generated, because it is inevitably affected by noise, in order to improve image quality and subsequent analysis accuracy, interference map filtering is required. The filtering algorithm will suppress noise interference based on the statistical characteristics of the interference graph while retaining effective phase information as much as possible. After the filtering is completed, the phase detangling process enters. Phase detangling is one of the key difficulties in InSAR data processing. The phase of the wound is reduced to the real phase value through the algorithm, so that the elevation and deformation information can be accurately calculated.

In this study, the treated partial interference vs. filtered differential interference diagram of the research area after the treatment is shown in Figure 8, which more clearly shows the interference characteristics of the research area. At the same time, the interference-to-coherence graph is shown in Figure 9. Coherence is an important indicator to measure the quality of InSAR data, which reflects the similarity of signals between the corresponding pixels of the main and auxiliary images. Comprehensive analysis of Figures 8 and 9 shows that the coherence of the land tent data in the study area is good, which means that the data quality is reliable and can provide a solid data foundation for subsequent accurate calculations of elevation and deformation.

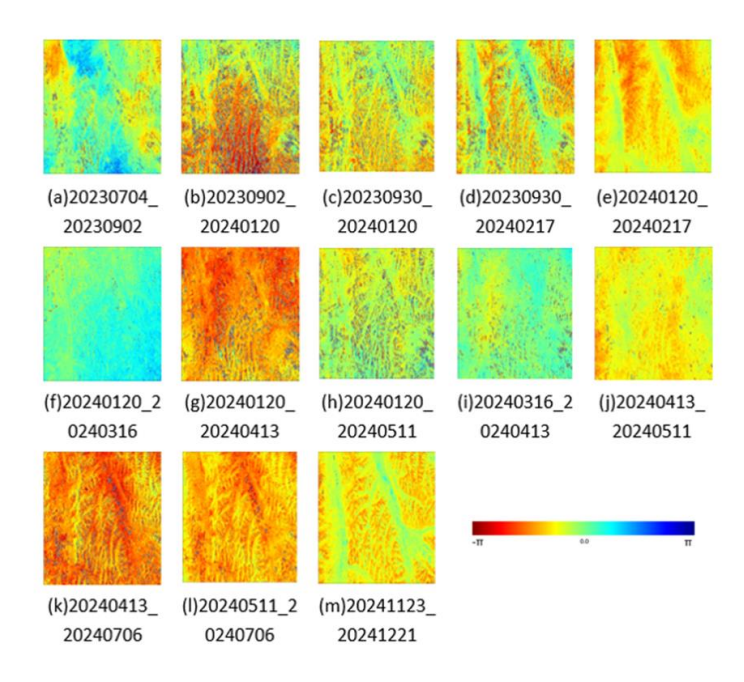


Figure 8. Partial filtered differential interferogram of the study area.

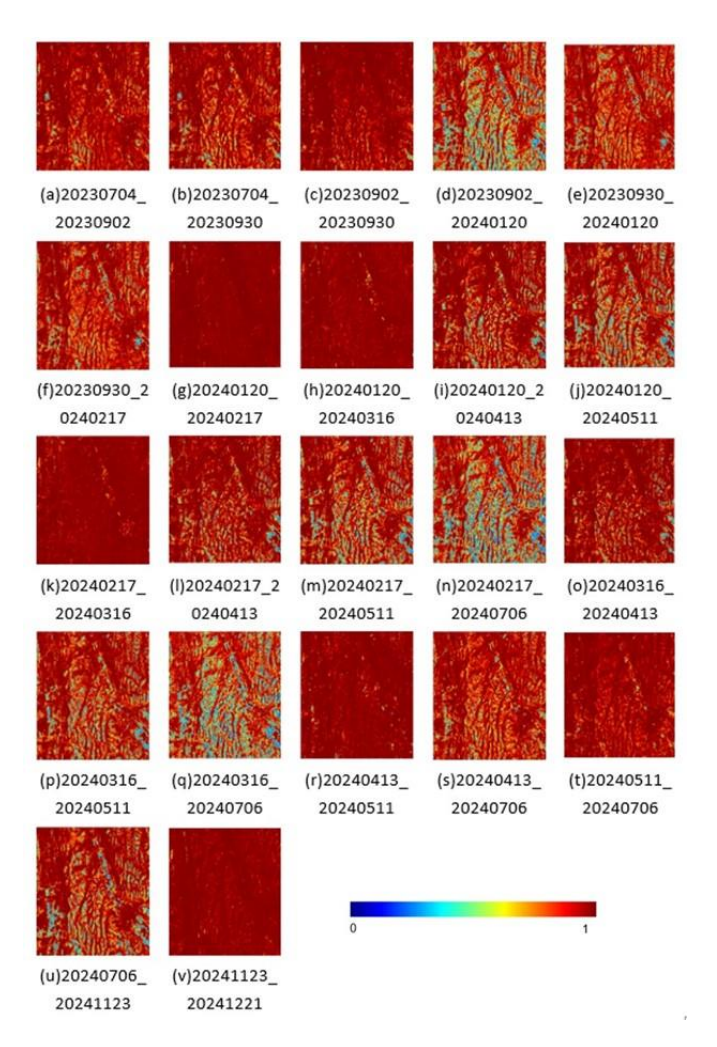


Figure 9. Coherence map of the Study srea.

#### 4.2. Deformation results and hidden danger analysis

After processing by SBAS-InSAR technology, the obtained deformation results are shown in Figure 10. The deformation result comprehensively presents the ground deformation status of the Huzhu Tu Autonomous County area, and its coverage covers the main geographical areas of the autonomous county, providing a macro perspective for the study of geological activity characteristics within the area. It can be clearly observed from Figure 10 that the study area is generally showing a relatively stable state, with the deformation variables in most areas at a low level, indicating that there has been no large-scale, universal drastic changes in the geological conditions in the area during the observation period. However, it is worth noting that there are still several more obvious deformation funnel areas in the figure. These areas are distributed in a relatively concentrated morphology, in sharp contrast with relatively stable areas around them. After detailed analysis and measurement, the maximum settlement in these deformation funnel areas has exceeded 100mm, which is beyond the normal deformation range, indicating that there may be potential geological disaster risks in these areas, such as ground collapse and foundation settlement, which require further in-depth research and targeted monitoring.

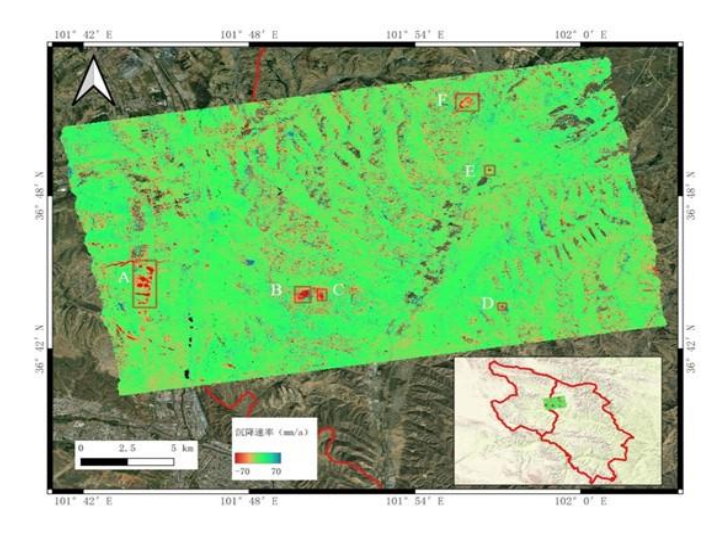


Figure 10. SBAS deformation rate diagram of LT-1 Data.

Figure 11 shows the geological disaster points in the corresponding geological disaster reservoir, including landslides, collapses and other disaster types. The investigation of geological disasters here is limited to areas where human activities such as cities, counties, villages, roads, scenic spots, etc. There is no investigation of geological disasters in deep mountains, dense forests, and wilderness. Therefore, the distribution of geological disasters in Figure 11 does not cover all treatment areas.

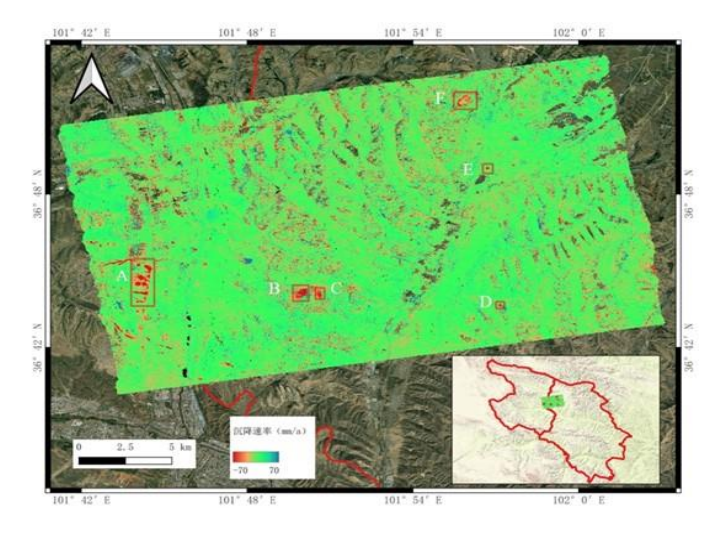
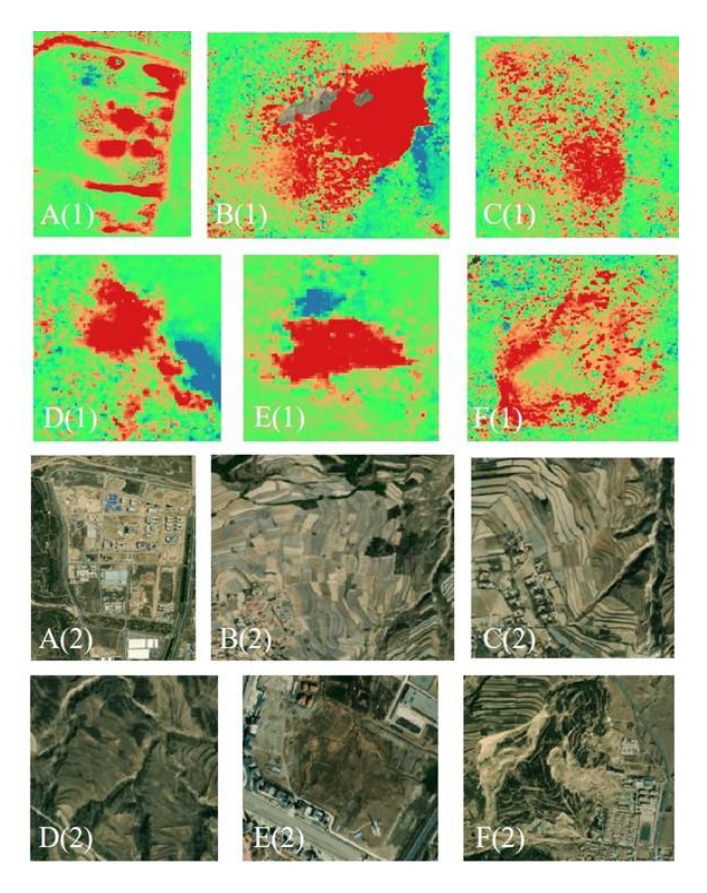


Figure 11. Geological disaster point distribution map.

In order to deeply analyze the reliability of the improved SBAS-InSAR technology during timing deformation inversion, we identified and extracted 6 effective deformation areas based on the deformation rate diagram obtained by this technology, as shown in Figure 12 (the specific position of each deformation is shown as a red rectangle in Figure 10). Afterwards, systematic cross-comparison is carried out with the historical geological disaster points and verified deformation areas in the geological disaster database. The results show that SBAS-InSAR technology can accurately capture subtle settlement changes in geological disaster points with its high spatiotemporal resolution and millimeter-level deformation monitoring capabilities, and also show extremely high consistency for the boundary identification and deformation trend analysis of known settlement areas. It is worth noting that this technology also has unique detection advantages and can keenly capture the periodic ground subsidence caused by human activities such as engineering

construction. For example, areas A and E provide important technical support for the investigation of geological disaster hazards and urban construction risk control.



**Figure 12.** Enlargement Results of Deformation Areas. (A-F) are the serial numbers of the deformation areas shown in Figure 10. (1) is the deformation result map of the area. (2) is the optical image of the area. The specific location of each deformation area is shown in Figure 10.

#### 4.3. Analysis of typical hidden dangers

Given the vast coverage of the research area, and geological disasters usually have small scale and local characteristics, it is difficult to accurately locate the corresponding deformation areas directly from large-scale data. To this end, this study comprehensively considered factors such as geological structure complexity, historical disaster records and human activity intensity, and finally selected four typical areas of Huzhu Tu Autonomous County, including Baoliu Village, Dazhuang Village, Sabaling and Xiafengtaigou (specific locations are areas B, C, D, and E in Figure 10 respectively), and carried out targeted analysis of geological disaster deformation characteristics, in order to provide an effective reference for the identification of large-scale geological disaster hazards through refined research on typical areas.

#### (1) Analysis of deformation results near Baoliu Village

Figure 13 shows the optical remote sensing diagram and deformation diagram near Baoliu Village, Huzhu Tu Autonomous County, and marks the deformation area with a red curve, which visually shows the ground settlement situation in the area. According to detailed data analysis, it can be seen that the maximum deformation variable in this area has exceeded 100mm, far exceeding the general settlement threshold; at the same time, through the comparison of timing deformation data, the ground settlement rate in this area is stable, and the overall trend of continuous and accelerated settlement has reached the level of severe settlement, and there are high geological disaster risks. We need to pay attention to it and carry out disaster prevention and mitigation work in a timely manner.

Through on-site investigation, there are large displacements in the terraced fields in the village, and cracks are present in the ridges, which show multiple groups of thin and short-line characteristics of different directions, which reduces the strength of the slope, poses a risk of instability, and poses a certain risk to the village.

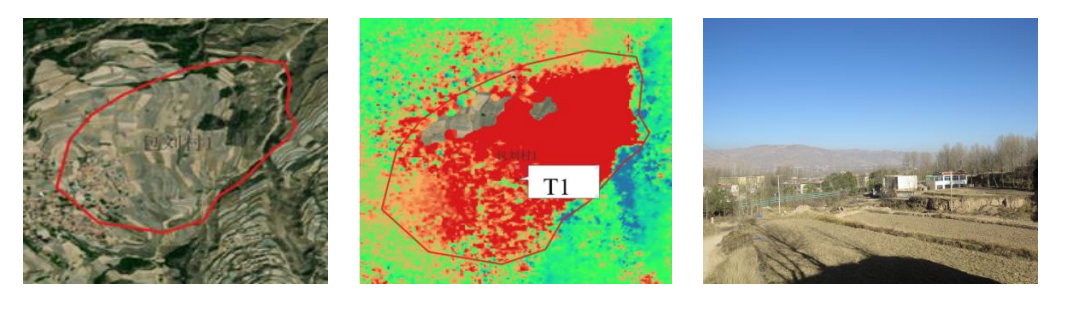


Figure 13. Optical images, deformation maps and on-site surveys near Baoliu Village.

Figure 14 draws the settlement trend chart of the T1 position in Figure 13, with the latitude and longitude of T1 (101.8318863°E, 36.7346649°N), located in the terraced field area on the northeast side of Baoliu Village. The horizontal axis of the chart is the time, starting from July 2023 until December 2024, and the vertical axis is the settlement amount (unit: mm). In the figure, the black scatter points represent the actual settlement data of each monitoring time point, and the red trend line intuitively shows the overall settlement trend. Its deformation rate is -63.074mm/a, and it is in the stage of continuous settlement as a whole. From the beginning of the first phase of monitoring to December 2024, a total of -104.76mm was settled.

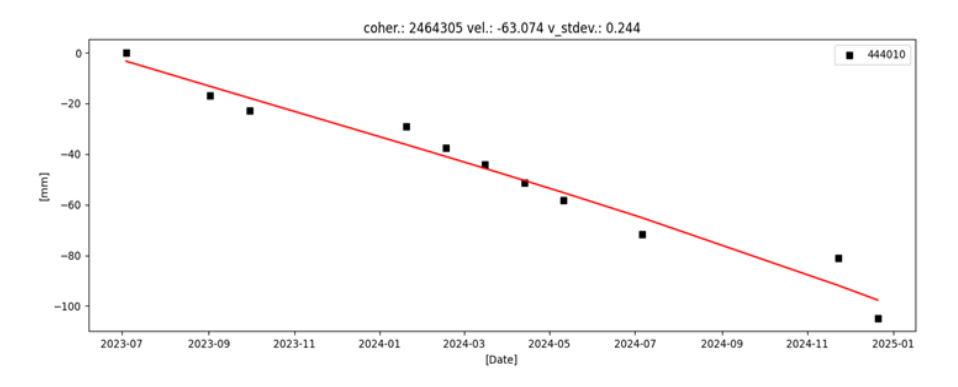


Figure 14. T1 settlement trend chart.

### (2) Analysis of deformation results near Dazhuangyi Village

Figure 15 shows the optical remote sensing image and deformation map near Dazhuangyi Village, with the deformation area marked by a red curve. The maximum deformation in the area also exceeds 100 mm, and the overall trend is continuous subsidence, classifying it as a severe subsidence area.



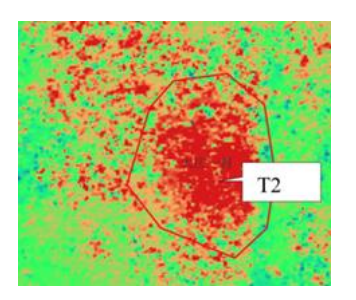


Figure 15. Optical images and deformation maps near Dazhuangyi Village.

Figure 16 draws the settlement trend chart of T2 position in Figure 15, with the latitude and longitude of T2 (101.8448334°E, 36.7339172°N), located in the terraced field area on the northeast side of Dazhuang Village. Its deformation rate is -55.269mm/a, and it is in the stage of continuous settlement as a whole. After the brief terrain lift began to occur during the first phase of monitoring, a total of -61.63mm was settled in December 2024.

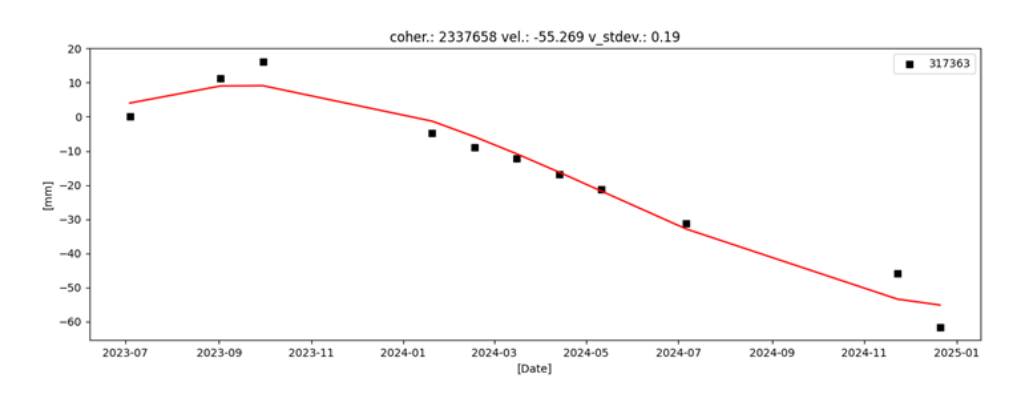


Figure 16. T2 settlement trend chart.

#### (3) Analysis of deformation results near Sabah Ridge

Figure 17 shows the optical remote sensing diagram and deformation diagram near Sabah Ridge, and marks the deformation area with a red curve. The maximum deformation in the area exceeds 80mm, and the overall trend of continuous settlement is shown, which belongs to the severe settlement area. Through on-site investigation, the slope body in this area has severe weathering and obvious slipping marks. The slope body has obvious staggering, and the joints are widely distributed, which increases the risk of slope instability.

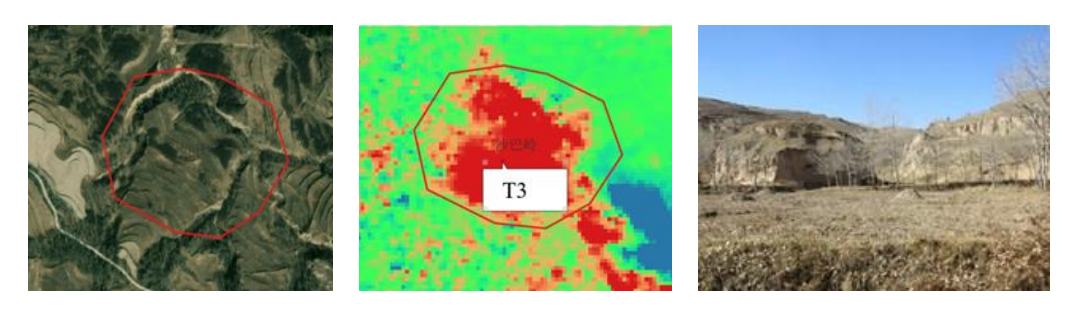


Figure 17. Optical images, deformation maps and on-site surveys near Sabah Ridge.

Figure 18 draws the settlement trend graph of the T3 position in Figure 17, with the latitude and longitude of T3 (101.9521255°E, 36.7277908°N), located in the central area of Sabah Ridge. Its deformation rate is -42.715mm/a, and it is in the stage of continuous settlement as a whole. From the beginning of the first phase of monitoring to January 2024, the surface deformation of the area remains relatively stable. Starting from January 2024, there will be continuous large-scale settlement in the area from December 2024, with the total settlement volume being -64.21mm.

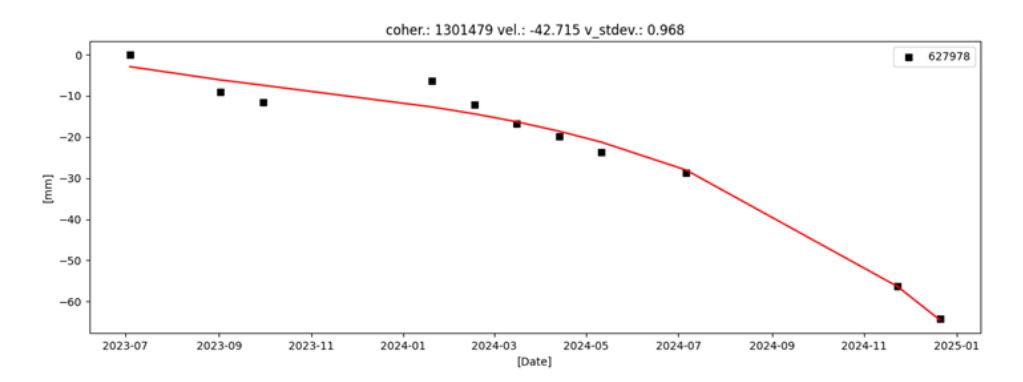


Figure 18. T3 settlement trend chart.

# (4) Analysis of deformation results near Xiafengtaigou

Figure 19 shows the optical remote sensing diagram and deformation diagram near Xiafengtaigou, and marks the deformation area with a red curve. The maximum deformation in the area exceeds 80mm, and the overall trend of continuous settlement is shown, which belongs to the severe settlement area.

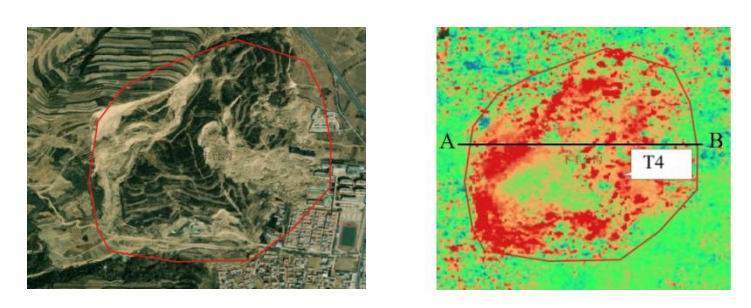


Figure 19. Optical images and deformation diagrams near Xiafengtaigou.

Figure 20 draws the settlement trend chart of the T4 position in Figure 19, with the latitude and longitude of T4 (101.9329758°E, 36.8602791°N), located in the hillside area on the east side of Xiafengtaigou. Its deformation rate is -49.051mm/a, and it is in the stage of continuous settlement as a whole. From the beginning of the first phase of monitoring to May 2024, the surface deformation remains relatively stable from May 2024 to November 2024, and then violent settlement occurs by December 2024, with the total settlement of -88.08mm.

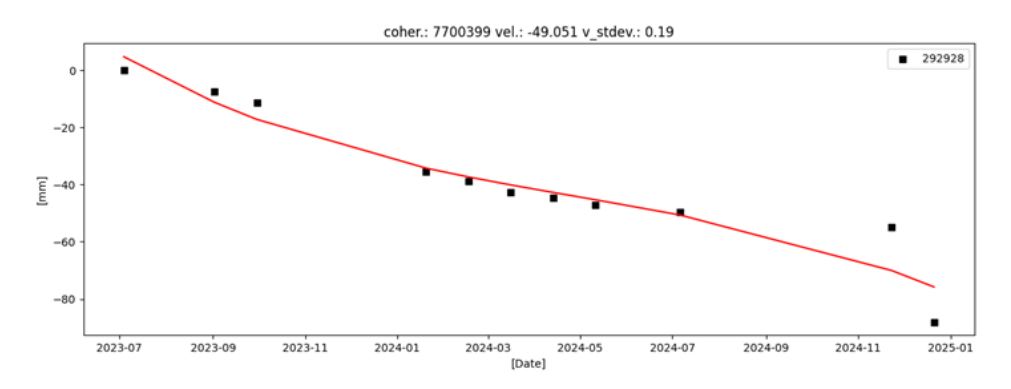


Figure 20. T4 settlement trend chart.

Figure 21 draws the deformation section curve diagram of the line segment AB in Figure 19. It can be seen that it has a large deformation on both sides and a small deformation in the middle, which is also highly consistent with the terrain of this area.

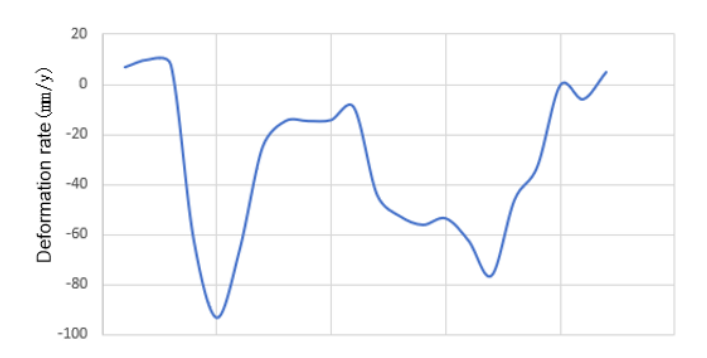


Figure 21. Deformation profile curve of AB line segment.

#### 4.4. Data comparison

In order to fully verify the accuracy of the Lu Investigation data, this study selected 47 Scenery Sentinel data from July 2023 to December 2024 as the verification benchmark. On the premise of ensuring that the SBAS-InSAR technology processing flow and parameter settings (including key parameters such as CS point selection threshold and track data correction) are completely consistent, the same research area is deformed, and the results are shown in Figure 22. By carefully comparing this result with the processing results based on land exploration data in Figure 10, it can be intuitively discovered that after the two data sources are processed by SBAS-InSAR technology, the identified deformation regions show high consistency in spatial distribution range and deformation-level change trends, which strongly proves the reliability and effectiveness of land exploration data in surface deformation monitoring applications.

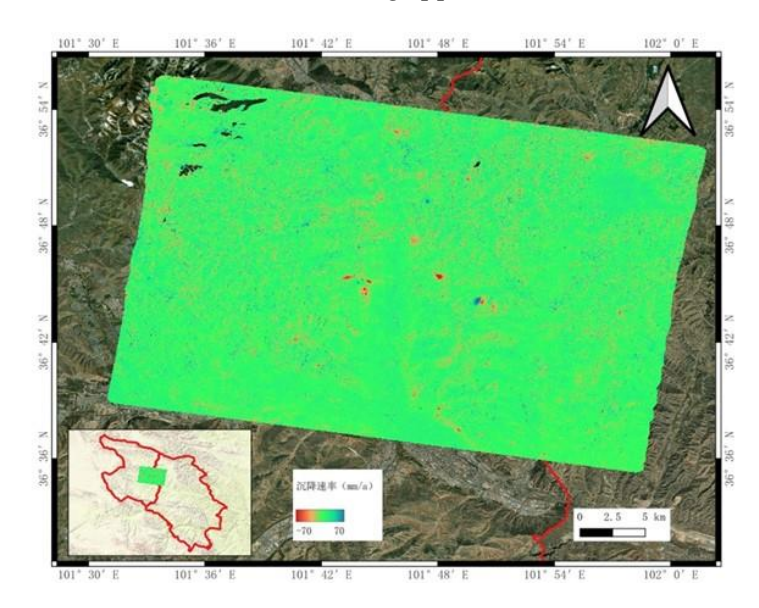
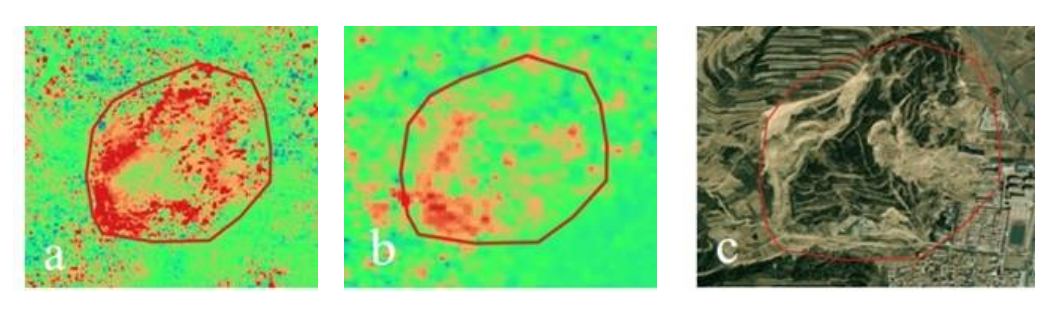


Figure 22. SBAS deformation rate diagram of sentinel data.

In order to further analyze the differences between land exploration data and sentinel data in deformation monitoring and accurately evaluate the performance of the two, this study selected the area near Xiafengtaigou, Huzhu Tu Autonomous County as a typical analysis sample, and conducted multi-dimensional cross-comparison of the deformation

results obtained by the two data with high-precision optical remote sensing images. Judging from the comparison results shown in Figure 23, the deformation monitoring results based on land exploration data show significant advantages: the outlined deformation boundaries are sharp and clear, and can accurately characterize the spatial range of ground settlement; the monitored deformation area is rich in details, and can capture tiny deformation characteristics and local abnormal changes, providing high-precision spatial information for the identification of geological disaster hazards. In contrast, the deformation results generated by sentry data are slightly inferior in terms of boundary clarity and detail presentation, the edges of the deformation area show blurring characteristics, and some subtle deformation signals are not effectively highlighted, and the detection capabilities in complex terrain and weak deformation scenarios are somewhat different from those of land exploration data. This comparison result intuitively verifies the high accuracy and strong adaptability of Land Detect data in the field of surface deformation monitoring, and provides strong data support for subsequent research and practical applications.



**Figure 23.** Deformation comparison near Xiafengtaigou. (a) shows the deformation results from LT-1 data. (b) presents the deformation results from Sentinel data. (c) is the optical image of this region.

In order to quantify the availability of the two data to the deformation results of the study area, the surface deformation points at the same coordinate position were randomly and uniformly sampled to determine the consistency of the annual deformation rate obtained by the two data. A total of 23,459 deformation rates of deformation points with the same geographical location were screened out, and in-depth correlation analysis was conducted on the annual average settlement rate, in order to reveal the consistency and differences in settlement monitoring under different data. The analysis results are shown in Figure 24. The settlement rate data obtained by the two data show extremely high correlation, with a correlation coefficient as high as 0.9143, showing a high consistency in the distribution of the annual average rate, which highlights the consistency and correlation between the two data in the monitoring results. This comparative analysis further confirms the accuracy of the land detect data in complex surface deformation monitoring.

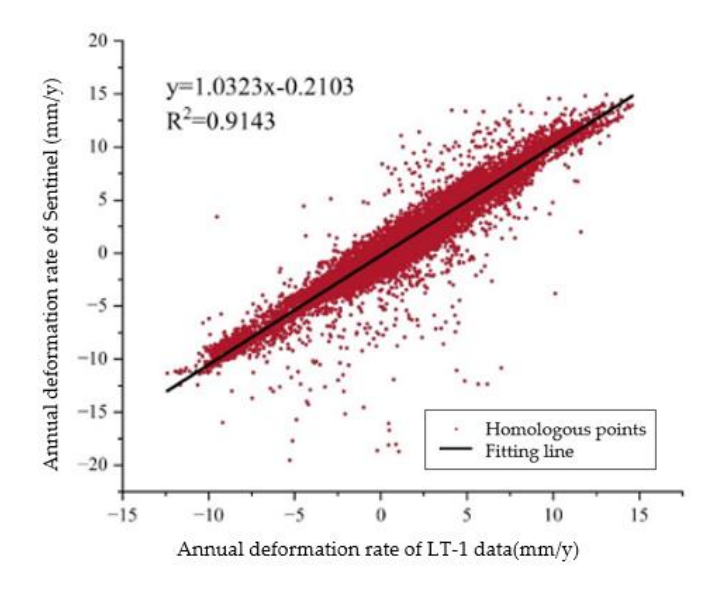
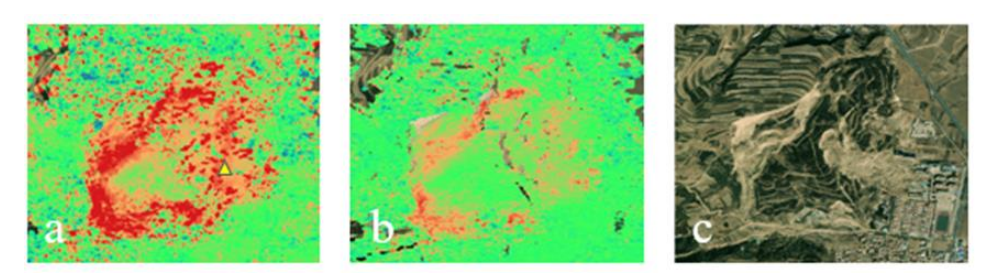


Figure 24. Select the scattered points of the homologous and the linear fitting relationship diagram.

#### 4.5. Accuracy verification

To clarify the subsidence monitoring effect of the improved SBAS algorithm proposed in this paper, deformation monitoring was respectively carried out on the study area using conventional SBAS technology and the improved SBAS technology based on LT-1 data. A typical subsidence area near Xiafengtaigou was selected as the comparison area, and its deformation rates are shown in Figure 25. From the distribution of different deformation states, the deformation rate results obtained by the two time-series InSAR methods are roughly the same in overall trend. It can also be seen that the improved SBAS can identify more monitoring points. Moreover, the improved SBAS technology monitors more deformation details, making the location of the subsidence area more obvious, while the deformation results obtained by the conventional SBAS technology have more blurred boundaries.

Additionally, the error comparison and correlation analysis of the deformation results between the two technologies are shown in Table 5. The standard deviation, root mean square error, and maximum error all meet the accuracy requirements for geological hazard monitoring. Meanwhile, the correlation coefficient of the deformation results between the two technologies is 0.896, indicating a strong positive correlation and good consistency in trends. Through the cross-validation of the two different deformation rate results, it is fully demonstrated that the improved SBAS technology is reliable in ground deformation monitoring.



**Figure 25.** Deformation rate maps near Xiafengtaigou. (a) Processing results of the improved SBAS (b) Processing results of the conventional SBAS (c) Optical image map

Table 4 Error Comparison and Correlation Analysis of Deformation Results between the Two Technologies

Metrics	Standard devi- ation	RMSE	Maximum er- ror	Correlation co- efficient
	1.352	2.125	3.23	0.896

To compare and verify the reliability of the data from the two techniques, a settlement characteristic point in the study area was selected for further cross-validation, and its location is indicated by the yellow triangle in Figure 25(a). The time-series settlement results obtained by the two techniques are shown in Figure 26. By comparing the data curves of the two techniques, it can be found that the trends of the settlement curves are relatively consistent with small errors. Additionally, the curve obtained by the improved SBAS is smoother, which indirectly reflects the effectiveness of this technique in monitoring surface deformation.

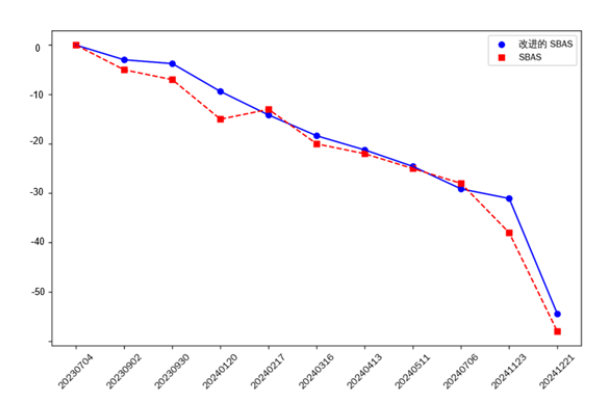


**Figure 26.** Comparison of Processing Results between Improved SBAS and Conventional SBAS Techniques

Subsequently, to further validate the accuracy of the monitoring results from the improved SBAS technology, the InSAR deformation measurement results were verified by integrating ground-based GNSS measurement results near Shabaling. Using three GNSS monitoring points (indicated by yellow triangles in Figure 27), their GNSS measurement results were projected onto the InSAR satellite line-of-sight (LOS) direction. The comparison results between the three groups of InSAR and GNSS measurements are shown in Figure 28, where circles represent the projection results of GNSS measurement data and triangles represent the InSAR deformation measurement results.



Figure 27. GNSS location map.

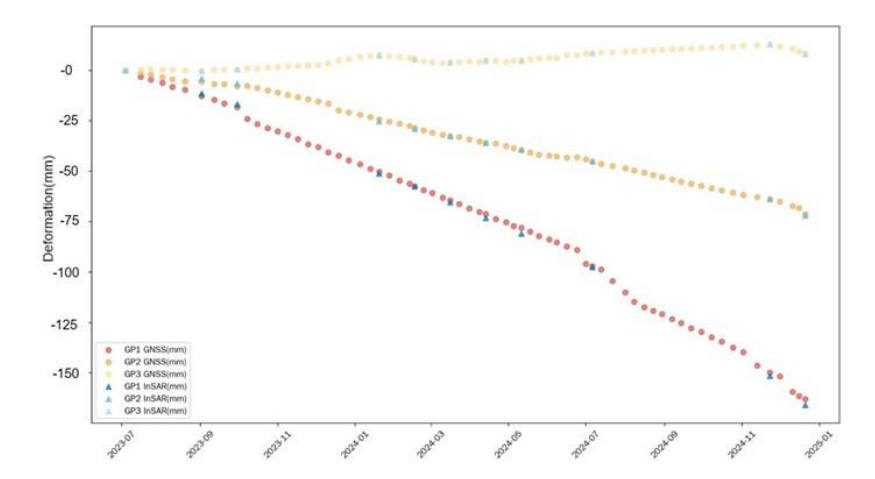


Figure 28. InSAR and GNSS comparison chart.

As shown in Figure 28, the InSAR measurement results are generally in good agreement with GNSS. Taking the cumulative settlement of each GNSS point measurement as the standard value and the InSAR monitoring results on the latest date as the measured value, the root mean square error (RMSE) of the cumulative settlement measurement at each point within the monitoring period is 3.45 mm, with the mean error of each point less than ±4 mm. The main difference is due to the slight deviation between the InSAR measurement points and the GNSS station locations, and the error is within an acceptable range, proving that the InSAR measurement results in the Shabaling Village area are reasonable.

To further illustrate the accuracy and reliability of deformation results obtained using LT-1 data with the improved SBAS-InSAR technique in the study area, statistical analysis was conducted on the standard deviation of surface deformation rates from March 2023 to February 2025, given the limited GNSS and leveling measurement data. Figure 29 shows the probability density function of deformation rate standard deviations for all monitoring points in the study area. The maximum standard deviation is 9.7 mm/a, and 98.2% of monitoring points have standard deviations below 5 mm/a, meeting the requirements of the InSAR Monitoring Technical Guidelines for Geological Hazards. Therefore, the deformation rate results for parts of Qinghai Province derived from LT-1 data processed using the improved SBAS-InSAR technique exhibit high reliability.

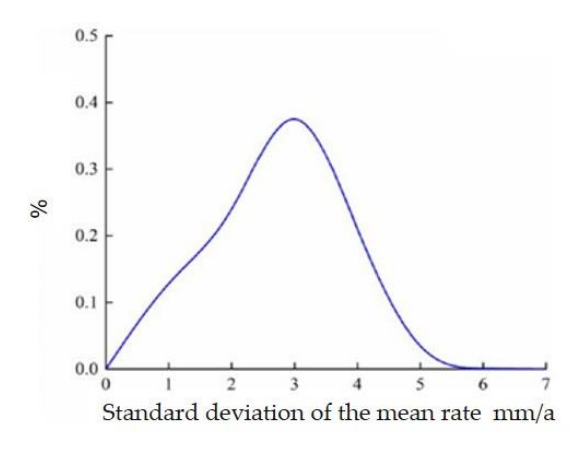


Figure 27. Probability density function graph of mean rate standard deviation.

#### 5. Discussion

This paper relies on domestic L-band differential interferometric SAR satellite data and uses SBAS-InSAR technology to achieve high-precision deformation inversion processing for some areas in Qinghai Province. During the processing, remote sensing optical image information and digital elevation model (DEM) data were fully integrated. Through cross-validation and comprehensive analysis of multi-source data, the spatial distribution of geological disaster hidden danger points in the region was accurately identified. To further verify the reliability of the method, the identification results were comprehensively and carefully compared with existing geological disaster databases and accurately mastered deformation areas. The comparison results show that the SBAS-InSAR technology has demonstrated high effectiveness in processing subsidence data, can more accurately capture ground deformation characteristics in the region, and provides a reliable technical means for the investigation of geological disaster hidden dangers.

The results of this research are of great practical significance and fully demonstrate the feasibility and practicality of InSAR deformation technology in a large-scale geological disaster census. This technology provides rich and accurate data support for relevant disaster prevention and mitigation departments, helping them to carry out disaster prevention, monitoring and governance more efficiently, and significantly improve geological disaster management and information service capabilities. At the same time, the obtained data also provides a solid and reliable data basis for in-depth analysis of the deformation mechanism of geological disasters and building a more accurate disaster warning model.

However, there is still some room for improvement in this study. On the one hand, due to the lack of precision orbit data of LT-1 data, this study refined the baseline of the LT-1 satellite interference map by selecting highly coherent ground control points, partially removing the impact of orbital system errors; the subsequent acquisition of precision orbit data can effectively improve the accuracy of monitoring deformation. On the other hand, the amount of data accumulated by the Land Disaster-1 satellite is relatively limited. Due to this constraint, it is difficult to conduct deformation analysis for longer time series, and it is impossible to have a more comprehensive and in-depth understanding of the long-term evolutionary laws of regional geological deformation. At the technical level, the SBAS-InSAR technology used in this article is relatively basic. If the data volume is sufficient in the future, more advanced technologies such as PSInSAR and DSInSAR can be introduced, which is expected to further improve the accuracy of deformation monitoring. In addition, if the InSAR lifting rail deformation results are fused, the three-dimensional deformation information of the ground can also be obtained, thereby achieving more refined monitoring and analysis of geological disaster hazard areas. Overall, although In-SAR deformation monitoring technology currently faces some challenges in its practical application, from a long-term perspective, it has shown great development potential in the field of geological disaster monitoring. With the improvement of satellite data acquisition capabilities and continuous technological innovation, it is expected to bring more significant benefits to geological disaster prevention and control work.

#### References

References must be numbered in order of appearance in the text (including citations in tables and legends) and listed individually at the end of the manuscript. We recommend preparing the references with a bibliography software package, such as EndNote, ReferenceManager or Zotero to avoid typing mistakes and duplicated references. Include the digital object identifier (DOI) for all references where available.

Citations and references in the Supplementary Materials are permitted provided that they also appear in the reference list here.

In the text, reference numbers should be placed in square brackets [] and placed before the punctuation; for example [1], [1–3] or [1,3]. For embedded citations in the text with pagination, use both parentheses and brackets to indicate the reference number and page numbers; for example [5] (p. 10), or [6] (pp. 101–105).

- Ding, X.; Montgomery, S.B.; Tsakiri, M.; Swindells, C.F.; Jewell, R.J. Integrated Monitoring Systems for Open Pit Wall Deformation; Meriwa Report No. 186; Australian Centre for Geomechanics: Perth, Australia, 1998.
- 2. Thompson, P.W.; Cierlitza, S. Identification of a slope failure over a year before final collapse using multiple monitoring methods. In Geotechnical Instrumentation and Monitoring in Open Pit and Underground Mining; Szwedzicki, T., Ed.; AA Balkema: Rotterdam, The Netherlands, 1993.
- 3. Carlo Colesanti, Alessandro Ferretti, et al. Monitoring landslides and tectonic motions with the Permanent Scatterers Technique[J]. Engineering Geology, 2003, 68: 3-14.
- 4. Usai S. A new approach for long term monitoring of deformations by differential SAR interferometry[D]. Delft Univ. of Tech, Delft, Netherlands, 2001.
- 5. Zebker H A, Villasenor J. Decorrelation in interfero-metric radar echoes. IEEE Transactions on Geosci-ence and Remote Sensing, 1992, 30(5): 950–959.
- 6. Bürgmann, Roland, Rosen P A, Fielding E J. Synthetic Aperture Radar Interferometry to Measure Earth's Surface Topography and Its Deformation[J]. Ann. rev. earth Planet, 2000, 28(1):169-209.
- 7. Ferretti A, Prati C and Rocca F. 2001. Permanent scatterers in SAR interferometry [J]. IEEE Transactions on Geoscience and Remote Sensing, 39(1): 8-20.
- 8. Ferretti, Alessandro; Prati, Claudio; Rocca, Fabio. Nonlinear subsidence rate estimation using permanent scatterers in differential SAR interferometry. IEEE Transactions on geoscience and remote sensing, 2000, 38, 2202-2212.
- 9. Hooper A., Zebker H., Segall P., et al. A new method for measuring deformation on volcanoes and other natural terrains using InSAR persistent scatterers[J]. Geophysical.
- 10. Vilardo G., Ventura G., Terranova C, et al. Ground deformation due to tectonic, hydrothermal, gravity, hydrogeological and anthropic processes in the Campanis Region (SouthernItaly) from Permannent Scatterers Synthetic Aperture Radar Interferometry[]]. Remote Sensing of Environment, 2009(113): 197-212.
- 11. Li S, Xu W, Li Z. Review of the SBAS InSAR Time-series algorithms, applications, and challenges[J]. Geodesy and Geodynamics, 2022, 13(2): 114-126.
- 12. Guo H, Yuan Y, Wang J, et al. Large-scale land subsidence monitoring and prediction based on SBAS-InSAR technology with time-series sentinel-1A satellite data[J]. Remote Sensing, 2023, 15(11): 2843.
- 13. Berardino P, Fornaro G, Lanari R, et al.A New Algorithm for Surface Deformation Monitoring Based on Small Baseline Differential SAR Interferograms[J].IEEE Transactions on Geoscience & Remote Sensing, 2002, 40(11):2375-2383.
- 14. Liu Y, Yang H, Fan J, et al. NL-MMSE: A hybrid phase optimization method in multimaster interferogram stack for DS-InSAR applications[J]. IEEE Journal of Selected Topics in Applied Earth Observations and Remote Sensing, 2022, 15: 8332-8345.
- 15. Ferretti A , Fumagalli A , Novali F ,et al.A New Algorithm for Processing Interferometric Data-Stacks: SqueeSAR[J].IEEE, 2011(9).
- 16. Zhang L, Gao P, Gan Z, et al. Surface subsidence monitoring of mining areas in Hunan province based on Sentinel-1A and DS-InSAR[J]. Sensors, 2023, 23(19): 8146.
- 17. Wang Y, Cui X, Che Y, et al. Automatic identification of slope active deformation areas in the Zhouqu region of China with DS-InSAR results[J]. Frontiers in Environmental Science, 2022, 10: 883427.
- 18. Ishwar S G, Kumar D. Application of DInSAR in mine surface subsidence monitoring and prediction[J]. Current Science, 2017: 46-51.
- 19. Fan H D, Cheng D, Deng K Z, et al. Subsidence monitoring using D-InSAR and probability integral prediction modelling in deep mining areas[J]. Survey review, 2015, 47(345): 438-445.
- 20. Yuan M, Li M, Liu H, et al. Subsidence monitoring base on SBAS-InSAR and slope stability analysis method for damage analysis in mountainous mining subsidence regions[J]. Remote Sensing, 2021, 13(16): 3107.
- 21. Wang Z, Zhao Y, Wang P, et al. Refined subsidence monitoring and dynamic prediction in narrow and long mining areas based on InSAR and probabilistic integral method[J]. Scientific Reports, 2024, 14(1): 28009.

- 22. Zhang J, Kou P, Tao Y, et al. Urban ground subsidence monitoring and prediction using time-series InSAR and machine learning approaches: a case study of Tianjin, China[J]. Environmental Earth Sciences, 2024, 83(16): 473.
- 23. Khan R, Li H, Afzal Z, et al. Monitoring subsidence in urban area by PSInSAR: A case study of Abbottabad City, Northern Pakistan[J]. Remote Sensing, 2021, 13(9): 1651.
- 24. Zheng Z, Xie C, He Y, et al. Monitoring potential geological hazards with different InSAR algorithms: The case of western Sichuan[J]. Remote Sensing, 2022, 14(9): 2049.
- 25. Yang F, Jiang Z, Ren J, et al. Monitoring, prediction, and evaluation of mountain geological hazards based on InSAR technology[J]. Scientific Programming, 2022, 2022(1): 2227049.
- 26. Bányai L, Bozsó I, Szűcs E, et al. Monitoring strategy of geological hazards using integrated three-dimensional InSAR and GNSS technologies with case study[J]. Periodica Polytechnica Civil Engineering, 2023, 67(4): 992-1000.
- 27. Shan X, Zhang G, Wang C, et al. Source characteristics of the Yutian earthquake in 2008 from inversion of the co-seismic deformation field mapped by InSAR[J]. Journal of Asian Earth Sciences, 2011, 40(4): 935-942.
- 28. Yang C, Han B, Zhao C, et al. Co-and post-seismic deformation mechanisms of the MW 7.3 Iran earthquake (2017) revealed by Sentinel-1 InSAR observations[J]. Remote sensing, 2019, 11(4): 418.
- 29. Yu C, Li Z, Chen J, et al. Small magnitude co-seismic deformation of the 2017 Mw 6.4 Nyingchi earthquake revealed by InSAR measurements with atmospheric correction[J]. Remote Sensing, 2018, 10(5): 684.
- 30. Chen Q, Liu X, Zhang Y, et al. A nonlinear inversion of InSAR-observed coseismic surface deformation for estimating variable fault dips in the 2008 Wenchuan earthquake[J]. International Journal of Applied Earth Observation and Geoinformation, 2019, 76: 179-192.
- 31. Zhang X, Feng M, Zhang H, et al. Detecting rock glacier displacement in the central Himalayas using multi-temporal In-SAR[J]. Remote Sensing, 2021, 13(23): 4738.
- 32. Liu L, Millar C I, Westfall R D, et al. Surface motion of active rock glaciers in the Sierra Nevada, California, USA: inventory and a case study using InSAR[J]. The Cryosphere, 2013, 7(4): 1109-1119.
- 33. Brencher G, Handwerger A L, Munroe J S. InSAR-based characterization of rock glacier movement in the Uinta Mountains, Utah, USA[J]. The Cryosphere, 2021, 15(10): 4823-4844.
- 34. Mahagaonkar A V. Glacier Surface Velocity Estimation and Facies Classification using InSAR and Muilt-Temporal SAR Techniques in Indian Himalaya[D]. University of Twente, 2019.
- 35. LI Y, LI Q, JIAO Q, et al. Application of Lutan-1 SAR Satellite Constellation to Earthquake Industry and Its Prospect[J]. Geomatics and Information Science of Wuhan University, 2024, 49(10): 1741-1752.
- 36. Li T, Tang X, Zhou X, et al. LuTan-1 SAR main applications and products[C]//EUSAR 2022; 14th European Conference on Synthetic Aperture Radar. VDE, 2022: 1-4.
- 37. Wang R, Liu K, Cai Y, et al. LuTan-1: An Innovative L-band Spaceborne Bistatic Interferometric SAR Mission[C]//EUSAR 2024; 15th European Conference on Synthetic Aperture Radar. VDE, 2024: 984-988.

**Disclaimer/Publisher's Note:** The statements, opinions and data contained in all publications are solely those of the individual author(s) and contributor(s) and not of MDPI and/or the editor(s). MDPI and/or the editor(s) disclaim responsibility for any injury to people or property resulting from any ideas, methods, instructions or products referred to in the content.